doi:10.26443/seismica.v5i1.1890

SEISMICA

Assessing creep event rheologies using their temporal evolution

Daniel B. Gittins * [1], **Jessica C. Hawthorne** [1]

[1]Department of Earth Sciences, University of Oxford, Oxford, UK

Author contributions: *Conceptualization*: Daniel B. Gittins, Jessica C. Hawthorne. *Methodology*: Daniel B. Gittins, Jessica C. Hawthorne. *Software*: Daniel B. Gittins. *Formal Analysis*: Daniel B. Gittins. *Writing - Original draft*: Daniel B. Gittins. *Writing - Review & Editing*: Daniel B. Gittins, Jessica C. Hawthorne. *Visualization*: Daniel B. Gittins. *Supervision*: Daniel B. Gittins. *Funding acquisition*: Daniel B. Gittins.

Abstract Aseismic creep events have been observed along the San Andreas Fault since the 1960s; yet, the fault properties that create these events still need to be identified. Here, we examine creepmeter data from events at Harris Ranch, CA, at the northern end of the San Andreas Fault's creeping section. We assess how well different rheological models describe the displacement-time evolution of surface-rupturing creep events. Using a basin-hopping approach, we minimise the misfit between the observed creepmeter data and predictions from five plausible rheological models for near-surface fault slip: 1) rate and state friction near steady state, (2) rate and state friction above steady state, (3) rate and state friction below steady state, (4) power-law flow, and (5) linear flow. We find most events are best fit by either a power-law flow or by rate and state friction below steady state. "Standard" velocity-strengthening friction models do not match the data well. This initial test of the rheologies could have one of several implications: (1) power-law creep somehow dominates even at near-surface conditions, (2) the near-surface is weak and mostly tracks the rheology of evolving slip at depth, or (3) a more complex rheology is required, perhaps including dilatancy or pore pressure evolution.

Non-technical summary Bursts of slip, or creep events, along the San Andreas Fault have been observed since the 1960s; however, it remains unclear what causes them to occur. To determine what is driving creep events, we compare the shape of creep events to five different models: (1) a frictional model where surface contacts change very slowly, (2) a frictional model where surface contacts break down quickly, (3) a frictional model where surface contacts strengthen, (4) a power-law flow model, and (5) a linear flow model. Most creep events are best described by a power-law flow or a frictional model where surface contacts strengthen. These results suggest additional work is required to understand the driving physics behind creep events, potentially incorporating more complex physical models than tested here.

Production Editor: Gareth Funning
Handling Editor: Matt Ikari
Copy & Layout Editor: Hannah F. Mark

Signed reviewer(s): Junle Jiang, Eric Lindsey

Received: July 24, 2025
Accepted: May 16, 2026
Published: May 24, 2026

1 Introduction

Aseismic creep along the 175 km-long central San Andreas Fault has been observed since the 1960s (Steinbrugge and Zacher, 1960; Tocher, 1960; Whitten and Claire, 1960). The aseismic slip along this creeping section occurs via slow, steady slip that is punctuated by a few-mm bursts of slip, known as creep events (e.g., Gittins and Hawthorne, 2022; Gladwin et al., 1994; Nason et al., 1974; Schulz, 1989). These creep events last a few hours to days and recur every few weeks or months (e.g., Gittins and Hawthorne, 2022; Gladwin et al., 1994; Schulz, 1989; Wei et al., 2013; Wesson, 1988).

Since Tocher (1960) first observed creep events, there have been various attempts to understand their behaviour. Researchers have estimated creep events' rupture extents (e.g., Bilham and Behr, 1992; Bilham et al., 2016; Burford, 1977; Evans et al., 1981; Gittins and Hawthorne, 2022; Gladwin et al., 1994; Goulty and Gilman, 1978; King, 2019; King et al., 1973; Nason and Weertman, 1973; Mchugh and Johnston, 1976; Mortensen et al., 1977; Slater and Burford, 1979) and have examined creep events' associations with rainfall (e.g., Roeloffs, 2001; Roeloffs et al., 1989; Schulz et al., 1983) and seismicity (e.g., Harris, 2017; Hirao et al., 2021; Khoshmanesh et al., 2015; Lyons and Sandwell, 2003; Nadeau and McEvilly, 2004; Thurber and Sessions, 1998).

Researchers have proposed several physical and rheological models to address the fundamental mystery of creep events: why slip accelerates but then stalls at low slip rates (e.g., Bilham and Behr, 1992; Nason and Weertman, 1973; Scholz, 1998; Slater and Burford, 1979; Wei et al., 2013; Wesson, 1988). Of particular interest here are some proposed rheological models — relationships between slip rate and fault strength — that could explain why creep events are always slow (e.g., Crough and Burford, 1977; Nason and Weertman, 1973; Scholz, 1998; Wei et al., 2013; Wesson, 1988).

In this study, we assess five proposed relationships between slip rate and strength — five rheological models — by examining the temporal evolution of slip during creep events. We assess whether the proposed mod-

*Corresponding author: tees.seis96@gmail.com

els predict slip evolution similar to that observed on surface creepmeter recordings.

The rheological models we test are (1) rate and state friction near steady state (at a constant state rate, $\dot{\theta} \approx$ a small constant), (2) rate and state friction above steady state (in a decreasing state regime, $\dot{\theta} < 0$), (3) rate and state friction below steady state (in a healing regime, $\dot{\theta} \approx 1$), (4) power-law flow, and (5) linear flow. Each of the proposed slip rate-strength relationships is motivated by plausible rock properties and conditions. For instance, we might expect near-steady state frictional sliding if the near-surface fault is frictional and slip rates change slowly.

By assessing which rheological models can match the data, we can take a step toward a physical understanding of creep events. Our assessment will, however, be constrained by a desire for simplicity. In this *step* toward physical understanding, we will use analytical models of slip that represent the rheologies' outcomes only in certain scenarios. These scenarios usually consider slip after a "kick": a step in stress, as described further in Section 3. Our modelling allows minimal spatial complexity in the creep event, and we return to this constraint in the discussion.

We describe the creepmeter data and event selection in Section 2, discuss the five rheological laws in Section 3, and describe how we fit these models in Section 4. We determine the percentage support of each rheology in Sections 5 and find that the two best-fitting rheological laws are a power-law flow model and rate and state friction below steady state (in a healing regime). Both of these rheologies turn out to be surprising, given our physical intuition for creep. In Section 6, we discuss the best-fitting model parameters, and in Section 7, we discuss the implications of the best-fitting rheologies for the driving mechanisms of creep events.

2 Data

We use creepmeter data from two iterations of the USGS creepmeter XHR at Harris Ranch, 11 km south of San Juan Bautista, CA (Figure 1), to investigate the driving rheology for creep events. The XHR2 iteration operated between 1991 and 2005 and was replaced by XHR3, which operated between 2009 and 2019. Each of these creepmeter iterations records at a sampling frequency of 10 minutes.

We use the creep event catalogue of Gittins and Hawthorne (2022) to identify and extract 113 creep events within the creepmeter record at XHR. These creep events typically last a few hours to days and have displacements of a few millimetres (Gittins and Hawthorne, 2022; Schulz, 1989). Figure 2 shows an example of a creep event recorded in December 1997, illustrating some of the key characteristics of creep events recorded at XHR. The majority of creep events at XHR have a sharp onset with little preamble (e.g., Bilham et al., 2004; Wesson, 1988). The gradient of the displacement-time curve is quite steep following this sharp onset but then rapidly decreases around the 'bend' of the creep event. After this sharp bend, little to no slip is recorded on the creepmeter, indicating the end of the creep event.

About two thirds of the creep events recorded at XHR actually have multiple phases of slip — multiple steps in the record (Bilham and Behr, 1992; Gladwin et al., 1994; Schulz, 1989; Wesson, 1988) — but for simplicity, we model only the 50 events that have one phase of slip. This subset of 50 events occurs across the whole time frame between 1991–2019 and does not show clustering in time.

3 Rheological Laws

3.1 General model: response of a velocity-strengthening fault to a kick in stress

Sections of faults near the surface are often found to be velocity-strengthening; fault strength typically increases with increasing slip rate (e.g., Marone et al., 1991; Scholz, 1990; Wei et al., 2013). As a result, near-surface fault sections—creeping sections—are thought to resist accelerations in slip. It thus seems plausible to imagine that in the absence of perturbations, the near-surface creeping section would slip at a steady rate close to plate rate, $\approx 10^{-9}$ ms^{-1}.

However, the stably sliding portion of the fault can receive an increase in stress from elsewhere, perhaps from above, in the form of rainfall-induced pore-pressure changes (e.g., Helmstetter and Shaw, 2009; Kanu and Johnson, 2011) or from below, from some slip at depth (e.g., Bilham and Behr, 1992; Gittins and Hawthorne, 2024; Slater and Burford, 1979). In this case, the fault may accelerate in response to the imposed stress. However, if a velocity-strengthening fault slips faster, its strength will increase, leading to a higher resistance to slip. That resistance stops acceleration and causes the fault to slow down. This acceleration and subsequent relaxation of the fault following a step increase in stress forms the basis of the 'kick' hypothesis for creep events.

The displacement in a creep event that arises from a 'kick' in stress depends on the fault zone rheology and the state of the fault when the kick occurs, i.e., on how well healed the fault is. We aim to determine which rheology and stress state best describes the displacement evolution of creep events.

We model the displacement evolution of creep events produced through different combinations of rheological laws and stress states. Here, we test three rheological laws: (1) rate and state friction, (2) power-law flow, and (3) linear flow. When testing the rate and state friction law, we must consider three scenarios, as the displacement evolution depends on how well-healed the fault is relative to its slip rate. These scenarios describe (1) a near-steady-state fault, with healing that matches the evolving slip rate, (2) an above-steady-state fault, which is overly healed relative to its slip rate, and (3) a below-steady-state fault, which is under-healed relative to its slip rate. The scenarios are described further in Section 3.3.1.

These combinations of rheological law and stress state provide us with a total of five rheological models with which to try and explain the displacement evo-

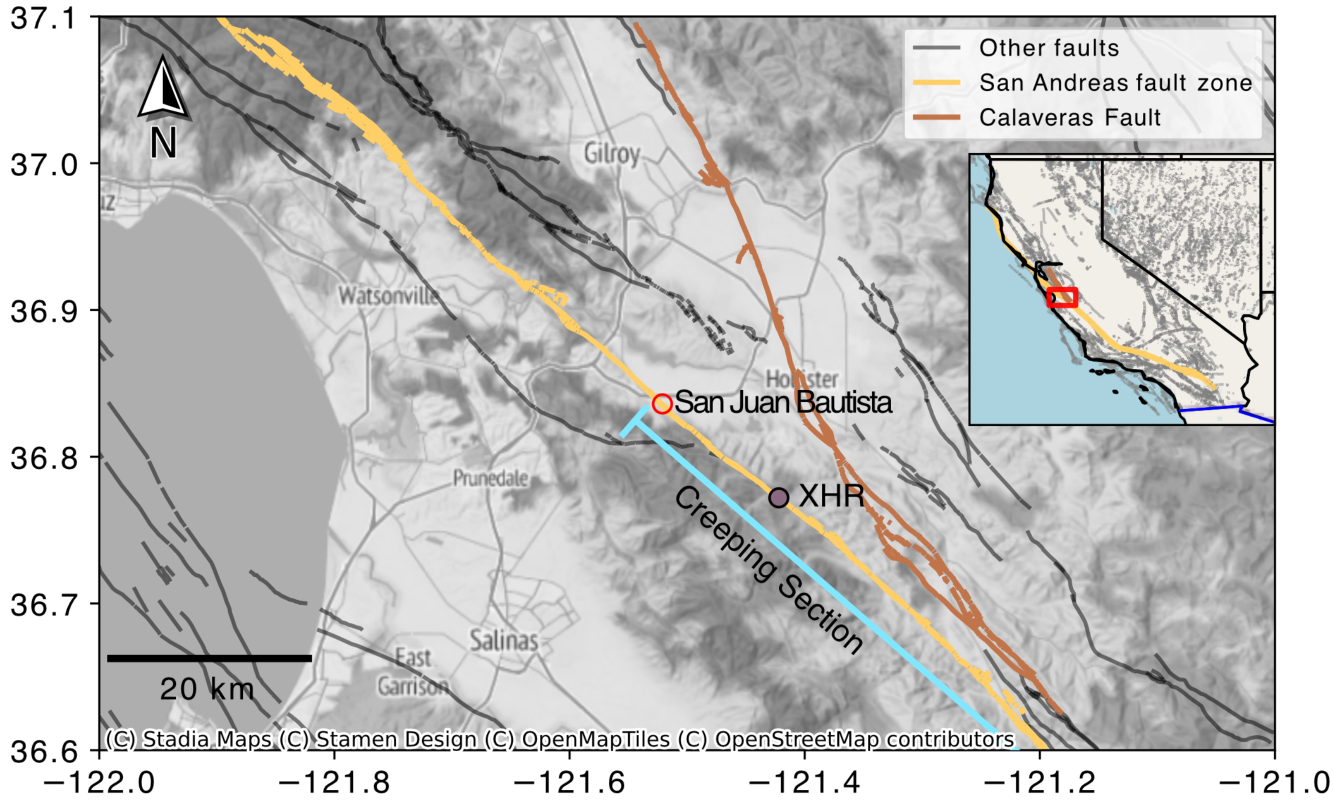

Figure 1 Map of the northern end of the creeping section of the central San Andreas Fault (yellow) and Calaveras Fault (Brown). Other faults in central California are shown in grey. The USGS creepmeter XHR is the purple circle. Faults plotted are from the USGS/California Geological Survey Quaternary faults and folds database (USGS and CGS, 2020). Inset shows the map location in the wider context of California, with faults having the same colours as the main map.

lution of creep events: (1) rate and state friction near steady state, (2) rate and state friction above steady state, (3) rate and state friction below steady state, (4) power-law flow, and (5) linear flow.

These rheological models are simple scenarios that could produce creep events. More complex models may better describe the evolution of slip in creep events; however, they do not have simple analytical solutions. Therefore, we test these simple models to see if any can describe the displacement evolution of creep events, providing a foundation for testing more complex models in the future.

3.2 Model component 1: Elasticity

The rheology of the patch is not the only determining factor controlling how the slip rate evolves with time. The elastic interactions of neighbouring fault patches also affect the slip rate. We will consider a simple model of elastic interactions. Here one patch of the fault slips in creep events. It is surrounded by neighbouring regions that slip at a steady rate. When the creep event patch slips faster than its surroundings, stress is pushed from the patch to its neighbours. The stress on the patch decreases, and the stresses on its neighbours increases.

A reasonable estimate of the rate of change of stress ($\dot{\tau}$) on the patch is given by a spring block slider model (Figure 3), where

$$\dot{\tau} = k(V - \dot{\delta}), \tag{1}$$

Here V is the slip rate of the surrounding regions, and $\dot{\delta}$ is the slip rate on the patch. k is an effective spring stiffness, which is proportional to the shear modulus of the material divided by the patch diameter (Dieterich, 1992; Perfettini and Avouac, 2004; Scholz, 1998).

3.3 Model component 2: Rate and state rheology

3.3.1 Rate and state definition

Now that we have a model for elastic stress interactions, we need a model for the local rheology of the fault: the stress-slip rate relationship. Given that creep events occur at shallow depths and low temperatures (e.g., Bilham and Behr, 1992; Gladwin et al., 1994; Wei et al., 2013), it is plausible that frictional processes control them. Here, we use the rate and state friction rheology (Ruina, 1983), which empirically approximates a number of laboratory experiments, starting from those of Dieterich (1979).

In the rate and state framework, the shear stress, τ, is a function of the slip rate, V, and the 'state' variable, θ:

$$\tau = \sigma\left[\mu^* + a\ln\frac{V}{V^*} + b\ln\frac{V^*\theta}{D_c}\right], \tag{2}$$

where σ is the normal stress, D_c is the characteristic sliding distance, μ^* and V^* are reference values of friction and slip rate, and a and b are the coefficients of the direct and evolution effect, respectively.

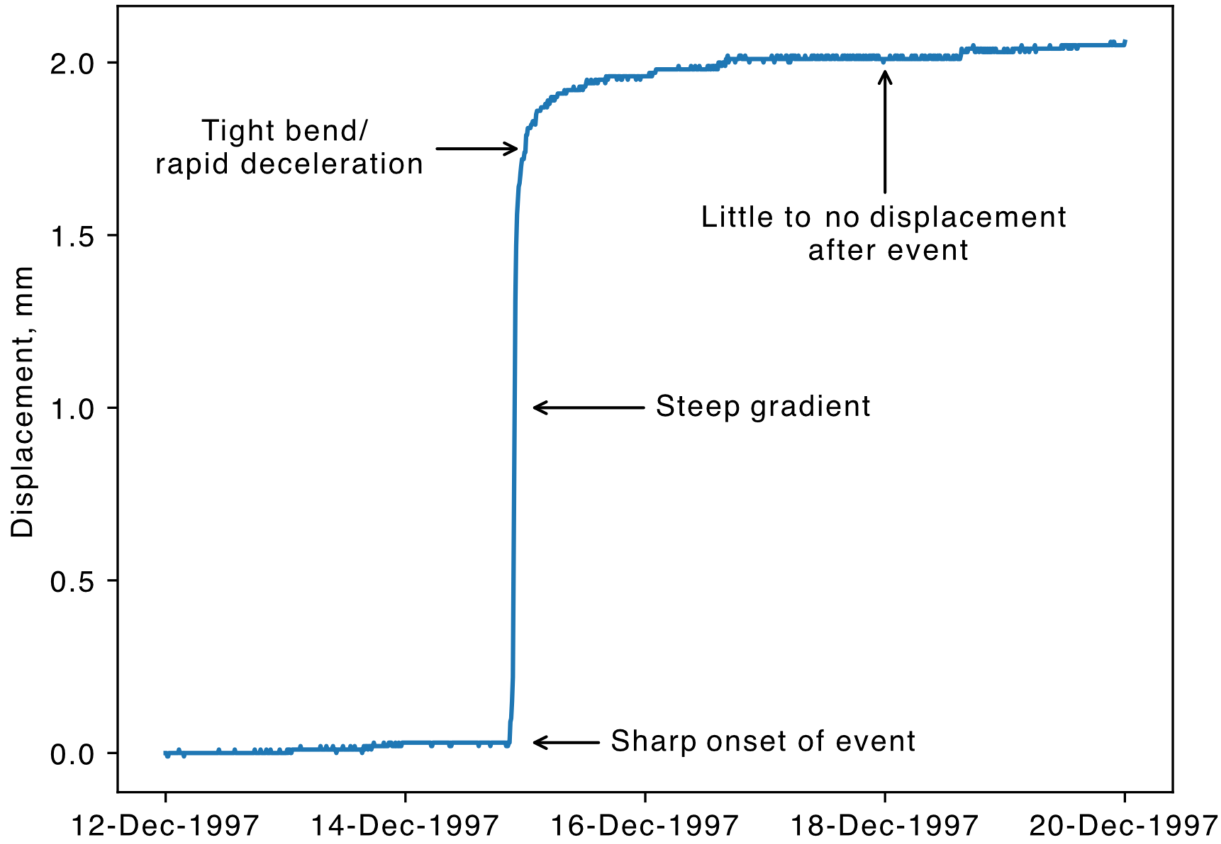

Figure 2 Example creep event recorded at XHR2 on 15th December 1997. Key features of the creep events recorded at XHR are highlighted.

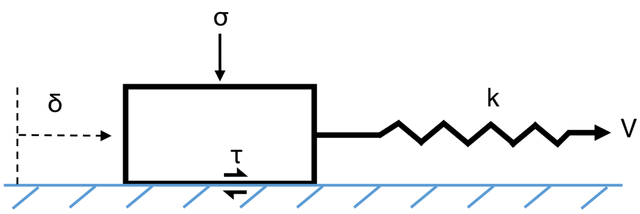

Figure 3 Spring block slider model.

The state variable θ can be thought of as an estimate of fault healing—perhaps as an estimate of the lifetime of small asperities on the fault surface, as θ has units of time. Asperities that last longer tend to grow more, and when asperities are more numerous and bigger, the fault is stronger, so a larger state θ implies an increase in fault strength. Asperities, and thus θ, can evolve with time and slip. Two evolution laws were proposed by Ruina (1983) to describe the rate of change of θ with time depending upon the slip rate, V, and a critical slip distance, D_c. The first of these is the aging law

$$\dot{\theta} = 1 - \frac{V\theta}{D_c}, \tag{3}$$

which was previously considered an appealing formulation because it predicts that fault surfaces strengthen on stationary contact, as was observed (e.g., Marone et al., 1991). The second state evolution law is the slip law

$$\dot{\theta} = -\frac{V\theta}{D_c} ln \frac{V\theta}{D_c}, \tag{4}$$

which does a better job than the aging law in modelling large changes in slip rate on laboratory faults (Beeler et al., 1994) and may be well suited to explaining the nucleation phase of slip (Ampuero and Rubin, 2008).

In practice, the slip law can also model laboratory-observed stress changes on apparent stationary contact and is likely a better "default" choice for frictional modelling (Bhattacharya et al., 2015, 2017). Unfortunately, analytical approximations of stress variations are often available only for the aging law (e.g., Helmstetter and Shaw, 2009). We thus choose to choose to use the aging law in this work; it is also a reasonable approximation of laboratory-observed stress variations, particularly near or below steady state (in the first and third scenarios below.)

3.3.2 Summary of rate and state scenarios

If a rate and state fault slips for a long time at a constant slip rate, it obtains a steady state in asperity distribution and healing: a value of θ consistent with long-term slip at that slip rate. The steady state value of θ is smaller for faster slip rates. One physical interpretation of this small θ is as a decrease in the size of asperities on the fault. Fault asperities are refreshed more quickly when the fault slips faster. They may thus have less time to grow and may be smaller, leading to a smaller θ.

However, if the fault slip rate changes abruptly, the asperities—and thus θ—may not be able to evolve quickly enough to remain near steady state. When we model displacement evolution in response to kicks in stress, we must note how quickly the stress changes. If the stress increases only moderately quickly, the fault asperity distribution will be able to change at the same rate. The asperities and thus the state will remain close to the "steady state" θ expected for the evolving slip rate and stress. The increase in stress will thus give rise to a fault that has relatively high stress but near-steady state conditions. Our first rate and state model considers the evolution of this fault, which turns out to follow the blue arrow in Figure 4a (Section 3.3.3).

In contrast, if the stress increases very quickly, the fault asperity distribution and thus the state θ may remain almost unchanged even as the fault stress and slip rate increase. This will give rise to a fault that is "above steady state". It is effectively over-healed relative to its slip rate. Our second rate and state model considers the evolution of this fault, which turns out to follow the red arrows in Figure 4 ($V\theta/D_c >> 1$, Section 3.3.4).

Finally, we many consider a scenario where stress decreases even as slip rate increases. Such a change is most plausible on a velocity-weakening fault, as illustrated in Figure 4b. This decrease may lead to a fault that falls "below steady state," as the fault becomes under-healed relative to its slip rate. Our final rate and state scenario considers this scenario, which turns out to follow the brown arrow in Figure 4b ($V\theta/D_c < 1$, Section 3.3.5).

3.3.3 Scenario 1: Constant state rate near steady state

Suppose the change in slip rate following an increase in stress occurs slowly relative to the timescale for the state evolution. This will give rise to a fault that is close to steady state. It turns out that after the step in stress, such a fault will follow a curve close to the blue arrow in Figure 4a. It will remain close to but slightly below steady state, with a nearly constant rate of increase in state θ (Helmstetter and Shaw, 2009).

In this model, creep events at the surface should record a near-steady-state relaxation following a step change in stress. This process is similar to that of afterslip. Within studies of afterslip, the system is often approximated to steady state (e.g., Helmstetter and Shaw, 2009; Montési, 2004), so that state is inversely proportional to the slip rate.

Here, however, we use the slightly more complete model, with a fault just a bit below steady state. In this model, the displacement occurring following a step change in stress evolves logarithmically with time (Helmstetter and Shaw, 2009; Marone et al., 1991; Scholz, 1990), such that

$$\delta(t) = V_0 t_{ss} ln\Big(1 + \frac{t - t_0}{t_{ss}}\Big), \tag{5}$$

where

$$t_{ss} = \frac{\sigma(a-b)}{kV_0}. \tag{6}$$

Here δ is the displacement, t is time, V_0 is the initial slip rate, t_{ss} is the characteristic time for displacement decay, t_0 is the initial time, and k is the spring stiffness (Helmstetter and Shaw, 2009).

3.3.4 Scenario 2: Above steady state

It is also possible to have more abrupt changes in stress. Suppose a step in stress causes a near-instantaneous change in slip rate. In this scenario, the "state" of the fault — the lifetimes, and thus the size and number of asperities — cannot change instantaneously. So, a large step in stress causes a step in slip rate with little change in state. This will give rise to a fault that is above steady state, starting at the beginning of the red arrows in Figure 4. Subsequently, state decreases, and asperities get smaller. The decrease in state causes a decrease in frictional resistance, which helps drive slip.

Although the slip law (Equation 4) is better at describing how the system behaves well above steady state, in this work, we use the aging law (Equation 3) following previous work to define how displacement evolves following a large step increase in stress (e.g., Helmstetter and Shaw, 2009; Rubin and Ampuero, 2005).

When the fault is well above steady state, the rate of change of state $\dot{\theta} \approx -\frac{V\theta}{D_c}$ (Dieterich, 1992; Helmstetter and Shaw, 2009). If a creep event patch slips in this regime, its displacement will accumulate as:

$$\delta(t) = V_0 t_1 ln\bigg(1 - \Big(\frac{t_a}{t_1}\Big)\Big(1 - e^{\frac{t-t_0}{t_a}}\Big)\bigg). \tag{7}$$

Here t_1 is given by

$$t_1 = \frac{a\sigma}{V_0(k - k_b)}, \tag{8}$$

with $k_b = \frac{b\sigma}{D_c}$ and t_a is given by

$$t_a = \frac{a\sigma}{\dot{\tau}_l}. \tag{9}$$

In Equations 7–9, t_a is the characteristic time of loading, t_1 is the charcteristic time of decay, $\dot{\tau}_l$ is the loading rate from the surrounding material, and k_b is the characteristic spring stiffness (Helmstetter and Shaw, 2009).

The above steady state regime does have a significant drawback when describing the slip evolution of creep events. As the fault slows down and state rate increases, the fundamental assumption that $\dot{\theta} \ll 0$, used to derive Equation 7, no longer holds (Helmstetter and Shaw, 2009). This means that Equation 7 becomes invalid in certain conditions, such as when the slip rate decreases toward the loading rate of the surrounding material.

In Figure 2, the slip rate following the bend of the creep event is low at $\approx 10^{-9}$ms^{-1}, similar to the loading rate. Therefore, the above steady state regime may only

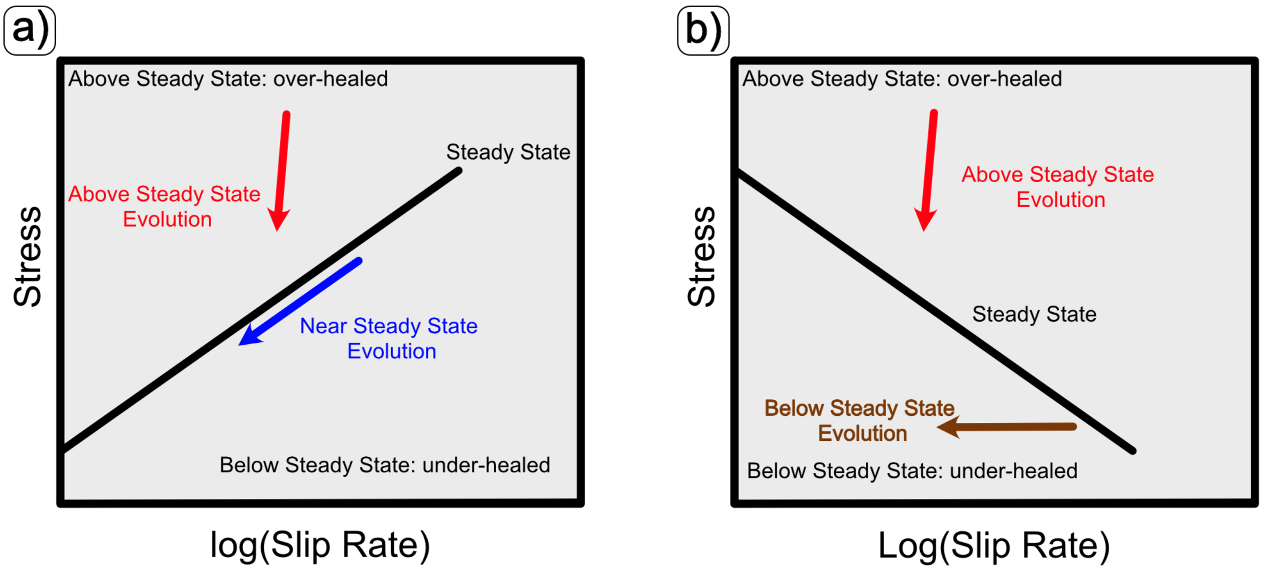

Figure 4 Schematic plot of slip rate against stress showing different evolutionary paths in: a) a velocity strengthening regime, and b) a velocity weakening regime. The beginning of each arrow is where the creep patch is assumed to start after the fault has received after the kick in stress. The slip and stress evolve following the arrows during the creep event. This evolution is what we model here.

be valid in the early stages of the creep event and poorly describe the displacement evolution at the end of the event, where slip rates are low.

3.3.5 Scenario 3: Below steady state

In the above steady state regime, the asperity sizes are getting smaller; θ is decreasing. However, it is also possible that significant slip occurs while state is increasing with time — when the fault is healing. During this healing phase, state increases; the lifetimes and sizes of asperities get bigger. However, if the fault slows down quickly enough—faster than asperities can grow—the fault will end up well below steady state, with $V\theta/D_c << 1$. Such a scenario is most plausible for a velocity-weakening fault, following the brown arrow in Figure 4b.

Such rapid deceleration might arise if the surface creep event we observe is just the end of a larger slip event that has propagated from depth. A velocity-weakening patch could nucleate a slip event at depth, which then propagates to the surface. By the time the event reaches the surface, most of the moment release in the event has already occurred. The whole system then decelerates together below steady state with only modest changes in stress.

We consider a particular case of fault healing when the slip rate decreases quickly enough that the fault is far below steady state so that $\dot{\theta} \approx 1$. Coupling this constraint with the modest changes in stress and a negligible loading rate, the slip in a creep event will evolve as

$$\delta(t) \approx \frac{V_0\theta_0}{b/a-1}\left[1-\left(1+\frac{t-t_0}{\theta_0}\right)^{1-b/a}\right], \qquad (10)$$

where θ_0 is the characteristic time (Helmstetter and Shaw, 2009).

3.4 Alternative Model Component 2: Power-law and Linear Flow Rheologies

We also attempt to model the displacement during creep events using flow laws. At first, describing creep events using flow laws may seem counter-intuitive. Flow laws are typically associated with deformation at high temperatures and pressures within the crust at depths near or below the brittle-ductile transition (Montési, 2004; Passchier and Trouw, 2005). Those conditions contrast with the shallow, cool conditions where creep events occur.

Nevertheless, we note that experiments on rocks that deform at high temperatures and pressures at depth often imply that effective fault slip rates V should scale as some power of stress:

$$V \propto \tau_a^n, \qquad (11)$$

where V is slip rate, τ_a is the applied stress, and n is determined by the the motion of intercrystalline dislocations (Passchier and Trouw, 2005). When stresses and strain rates are relatively high, n = 3–5 and deformation occurs through grain boundary sliding accommodated by dislocation creep (Hirth and Kohlstedt, 2004; Montési, 2004). When stresses are relatively low, n = 1 and deformation occurs through grain boundary sliding accommodated by diffusion creep (Evans and Kohlstedt, 1995; Hirth and Kohlstedt, 2004; Montési, 2004).

Empirically derived laws for the displacement evolution of creep events by Crough and Burford (1977) and later modified by Wesson (1988) have a similar functional form to the flow laws. This similarity also encourages us to include flow laws in our analysis. Further, these flow laws sometimes have a similar form to those for describing pressure solution creep, a process that might explain shallow aseismic creep (Gratier et al., 2011; Richard et al., 2014). We discuss the feasibility of this process for explaining the displacement observed in creep events further as part of the discussion in Section 7.1.

If the near-surface fault is governed by power-law flow, and it experiences an abrupt 'kick' in stress, slip at the surface will evolve as:

$$\delta(t) = \delta_0 + V_0 t_c n\Big[1 - \Big\{1 + \Big(1 - \frac{1}{n}\Big)\Big(\frac{t - t_0}{t_c}\Big)\Big\}^{\frac{1}{1-n}}\Big], \quad (12)$$

where t_c is the time constant and n is the power-law exponent (Montési, 2004).

When n = 1, Equation 12 reduces to the linear flow model

$$\delta(t) = \delta_0 + V_0 t_c\Big(1 - e^{\frac{t-t_0}{t_c}}\Big). \quad (13)$$

4 Fitting the shape of the events

Physical analysis thus suggests five ways that slip might accumulate during creep events (Equations 5, 7, 10, 12, and 13). We now aim to assess which, if any, of these equations accurately match the data and which parameters are required.

4.1 Forward Model

Sometimes the creep rate increases slightly before the main phase of the creep event. The displacement that accumulates, or preamble, is due to strain related to the approach of a subsurface dislocation before the commencement of slip at the creepmeter site (King et al., 1977) and is not part of the creep event itself. So, we model the observed displacement in two parts: a preamble that includes a constant slip rate, and a main phase that incorporates the rheological models. We determine the best-fitting parameters for each rheological model using a two-part fit. This two-part fit includes a straight line and the displacement described by the rheological model, such that

$$\delta = \begin{cases} \delta(t) = V_b t + Q, & t \leq T_{01} \\ \delta(t) = V_b t + Q + \delta_r(t), & t > T_{01} \end{cases}. \quad (14)$$

In Equation 14, $\delta(t)$ represents the observed displacement with time, t.

We note, however, that there are sometimes long-term trends in the data that we need to account for.

For the slip prior to the onset of the creep event, at $t = T_{01}$, the displacement is calculated using V_b, the slip rate in the few hours before the creep event, and Q, a constant allowing for a straight line to be fit to the time T_{01}. When $t > T_{01}$, we add to this the rheology-dependant displacement evolution, $\delta_r(t)$ which is based upon Equations 5, 7, 10, 12, & 13.

4.2 Creepmeter Noise Estimates

When assessing whether the modelled slip matches the data, it is important to account for noise in data. The noise is temporally correlated: there is covariance between displacement at one time and displacement at a later time. Such red noise is typical of noise in creepmeters and other high-precision geodetic time series, which are dominated by hydrology, pressure, and settling behaviours (e.g., Langbein et al., 1993; Langbein and Johnson, 1997).

To estimate the temporal covariance of the noise, we select 50,000 segments of creepmeter data that are four days long. These segments are representative of the noise in the data. They possess no data gaps and contain no creep events, but they do contain creep variations associated with rainfall, hydrology, and instrument errors. To quantify the magnitude of these variations, we aim to compute the covariance between creep values at various times within each record. Specifically, we aim to compute a set of covariances C_{mn} by computing the expected values of the multiplied noise observations:

$$C_{mn} = E\left[d(t_n) - d(t_0))(d(t_m) - d(t_0)\right]. \quad (15)$$

Here d are creep observations, t_0 is the segment start time, and t_m and t_n are times within the segment. This expected value is the mean value of $(d(t_n) - d(t_0)) \times (d(t_m) - d(t_0))$ that one would expect if one extracted a segment of creepmeter noise at random.

To obtain the expected value for a given t_m-t_n pair, we simply consider all of the available 50,000 noise segments. We extract the value $(d(t_n) - d(t_0)) \times (d(t_m) - d(t_0))$ from each segment and average the available 50,000 values. Repeating this procedure for all m-n pairs gives a noise covariance matrix C, with elements C_{mn} (e.g., Hawthorne and Rubin, 2013). We calculate one data covariance matrix for each version of the installed XHR creepmeter (i.e., one for XHR2 and one for XHR3).

The covariance matrices are shown in Figure 5; they capture the largest uncertainties in the data. From these covariance matrices, we can see that large random walk noise is present in the data. The noise covariance C_{mn} gets larger further away from the origin—the segment start time—including large values away from the diagonal. Such values imply that $(d(t_n) - d(t_0)) \times (d(t_m) - d(t_0))$ increases as t_m and t_n increase. In other words, the creep $d(t_n)$ tends to wander farther from its original value $d(t_0)$ when it has a longer time interval $t_n - t_0$ (see also Langbein and Johnson, 1997; Langbein, 2004; Williams et al., 2004).

However, even an average of 50,000 segments misses small details of the covariance matrix. Noise in our estimates means that the calculated covariance matrices have a few negative eigenvalues. To regularise the covariance matrices and make them invertible, we add a component of white noise to the covariance matrices, with an amplitude of $0.1 \times \mathbf{C}_{22}$, where $\mathbf{C}_{22}$ is the second value along the matrix diagonal.

4.3 Misfit Calculation

Now that we know the uncertainty on the data, we can assess the accuracy of any modelled displacement, $\delta(t)$. To do this we need to define a function that will assess the misfit of $\delta(t)$ to the observed data. We define this misfit function as:

$$\text{Misfit} = \frac{(\delta_{obs}(t) - \delta(t))^T \cdot \mathbf{C}^{-1} \cdot (\delta_{obs}(t) - \delta(t))}{\delta_{obs}(t) \cdot \mathbf{C}^{-1} \cdot \delta_{obs}(t)}, \quad (16)$$

where $\delta_{obs}(t)$ and $\delta(t)$ are the observed and modelled slips, respectively, and C is the noise covariance matrix.

4.4 Parameter Search

In the parameter search, we go from event to event and try to find the best parameters for each of the models. To find the parameters with the lowest misfit, we minimise Equation 16 using a two-step approach.

We first fit the data with a rapid Sequential Least Squares Programming (SLSQP) algorithm (Kraft, 1988; Lawson and Hanson, 1995; Nocedal and Wright, 2006). This algorithm models the misfit sequential, with different sets of quadratic functions. It allows us to get a reasonable result quickly without needing a good initial guess for the parameters. The initial possible range of parameter values is allowed to be quite large. We set all time constants (t_c, $t_s s$, t_a and θ_0) to be between 1–100, n to be between 1–5, t_1 to be between 1–10, and b/a to be between 0–10. We chose these values to allow for a wide range of possible parameters. Previous studies on the rheology of creep events (e.g., Crough and Burford, 1977; Wesson, 1988) did not use the rheologies tested here, so no best guess for the initial parameters from previous work could be used. During the fitting process we allowed the start and end times of the fitting section and T_{01} to vary by $\pm$ 30 minutes (i.e., 3 data points either side). We chose this range to account for errors in picking of the start (T_{01}) and end times in Gittins and Hawthorne (2022). This initial fitting converges well for the models with power-law flow, linear flow, and rate and state friction below steady state.

However, for both rate and state friction at a constant state rate near steady state and rate and state friction above steady state, the SLSQP algorithm converges to a poor fit, failing to match the middle of the creep event. The output of the SLSQP algorithm is then used as an initial guess for a more precise fitting using a Nelder-Mead algorithm (Nelder and Mead, 1965), which is closer to gradient descent and converges quickly. We use this two-stage approach because using Nelder-Mead alone leads to unsatisfactory fitting due to poorly constrained initial conditions. These poorly constrained initial conditions lead the Nelder-Mead algorithm to often converge to somewhat broad local minima.

5 Determining the best-fitting models

All of the rheologies can match the rough shape of the creep events. Figure 6 shows six examples of the modelled slip. However, some rheologies visibly match the data better and have smaller misfits.

Not all models are created equally. Some have extra free parameters. Therefore, we need to discriminate between models based on the misfits, while also penalising models with extra free parameters. To do this we use the Akaike Information Criterion (AIC) (Akaike, 1973, 1998).

5.1 Akaike Information Criterion

The AIC (Akaike, 1973, 1998) is an estimate of the capability of a model to predict as set of values in the data. It is defined as

$$AIC = 2m + N \cdot \ln\left(\frac{RSS}{N}\right), \quad (17)$$

$$RSS = \sum_i (\delta_{obs}(t) - \delta(t))^2, \quad (18)$$

where N is the number of observations, m is the number of model parameters, and RSS is the residual sum of squares.

We use the AIC to provide a framework for comparing our five models. It is capable of comparing between both nested (linear and power-law flow) and non-nested models. Unlike traditional hypothesis tests such as the F-test, AIC quantifies the relative quality of statistical models by: (1) rewarding models that fit the data well; (2) penalising models with more parameters to avoid over-fitting, and (3) allowing direct comparisons across models regardless of their nested relationships.

5.1.1 Adapting the misfit for AIC calculation

In our initial calculations, we chose to normalise the error in the model by the variability in the data to obtain intuitively interpretable numbers (Equation 16). However, this normalisation is not compatible with AIC, which requires an absolute measure of model misfit analogous to residual sum of squares. For AIC, we simply calculate the residual sum of squares:

$$RSS_w = (\delta_{obs}(t) - \delta(t))^T \cdot \mathbf{C}^{-1} \cdot (\delta_{obs}(t) - \delta(t)) \quad (19)$$

This equation is a scaled version of Equation 18.

5.2 Comparing models using AIC

We calculate the AIC for each event using each of the five proposed models, or rheologies. Then we assign each event a best-fitting rheology, based on which model has the lowest AIC. To assess the confidence in the rheology selection, we compute a ΔAIC for each rheology: the difference between each model's AIC and the minimum AIC value.

A simple approach for interpreting the AIC values would be to say that the best fitting model is the one with the lowest AIC and a $\Delta AIC = 0$. However this does not account for closely fitting models that have similar AIC values (e.g., $\Delta AIC \leq 2$). Only 18% of events have clear best-fitting models. Therefore we need a more sophisticated way of determining which model has the most support for describing the displacement evolution of creep events: Akaike weights.

5.2.1 Calculating Akaike weights to quantify relative model support

Akaike weights convert the AIC values calculated into probabilistic support for each model (Akaike, 1973, 1998; Wagenmakers and Farrell, 2004). Here, although

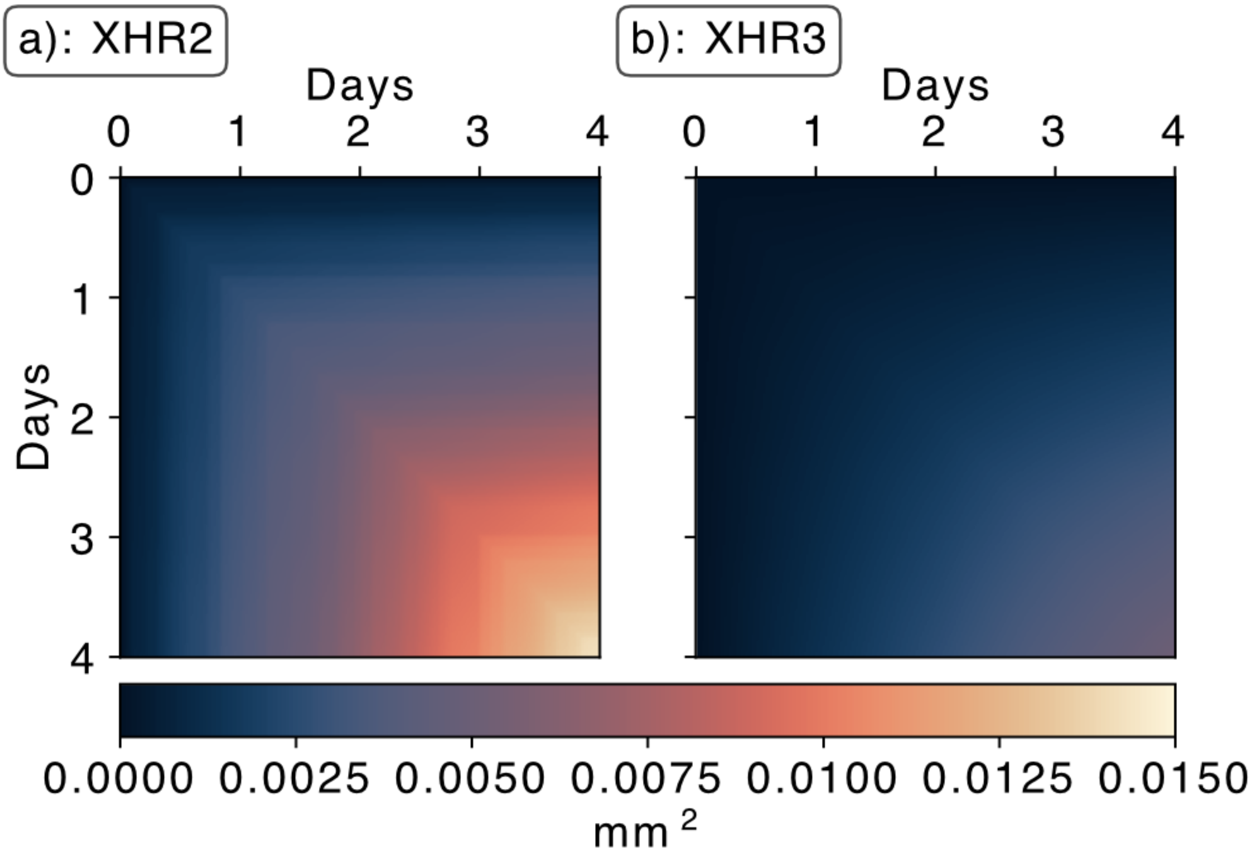

Figure 5 a) The covariance matrix of the earlier XHR2 creepmeter (1992 and 2005). b) The covariance matrix of the later XHR3 creepmeter (2009 and 2019). Note that XHR3 has lower noise than XHR2.

the model with the lowest AIC is considered the best, the differences (ΔAIC) between models matter most. The Akaike weight for model i, w_i, gives the relative likelihood that model i is the best among all models, given the data. The weights of all five models sum to one and are defined as the relative likelihood of model i over the sum of the likelihoods of all models:

$$w_i = \frac{e^{-0.5\Delta AIC_i}}{\sum_j e^{-0.5\Delta AIC_j}}. \tag{20}$$

These Akaike weights allow us to compare models probabilistically. They quantify the amount of support each model has for each event event. This approach allows us to: (1) account for uncertainty arising from the differing numbers of parameters in each model and (2) share support between models rather than picking one "best fitting" model. These weights are then used to determine the support for each model. For example if one model has $w_i = 0.9$, it is overwhelmingly supported. However, if one model has $w_i = 0.45$ and another $w_i = 0.4$, both are plausible. If many models have similar weights for a given creep event, there is no strongly preferred model.

Akaike weights provide a per-event estimate of how likely each model is to be the best. However, to understand the driving physics behind creep events as a whole we assess which model has the most support across events. To do this, we sum the Akaike weights for each model to get the total weights for the model and express this as a model support percentage. We then estimate the 70% uncertainty by bootstrapping the events included in the average. These bootstrapping results are shown in Figure 7a.

5.2.2 Adjusting the Akaike weights for power-law and linear flow

Before we interpret the summed Akaike weights, however, we may note that linear flow is a nested variant of power-law flow when $n = 1$. By including both of these models, we may be obscuring the competition between power-law flows and rate-and-state models. If power-law flow is primarily trading off against linear flow, then including both will reduce the comparative model support relative to the rate-and-state models. The more interesting question here is whether power-law flow performs better than its frictional counterparts?

In order to investigate this, we remove linear flow model from contention and recalculate each model's ΔAIC & w_i for each event. We then conduct the same bootstrapping approach as before to estimate the 70% confidence range for each model's support (Figure 7b).

5.3 Results of AIC comparisons

Below we discuss the model support percentages for each of the rheological models in order of the most to least supported model. We discuss these model support percentages when linear flow is included and excluded.

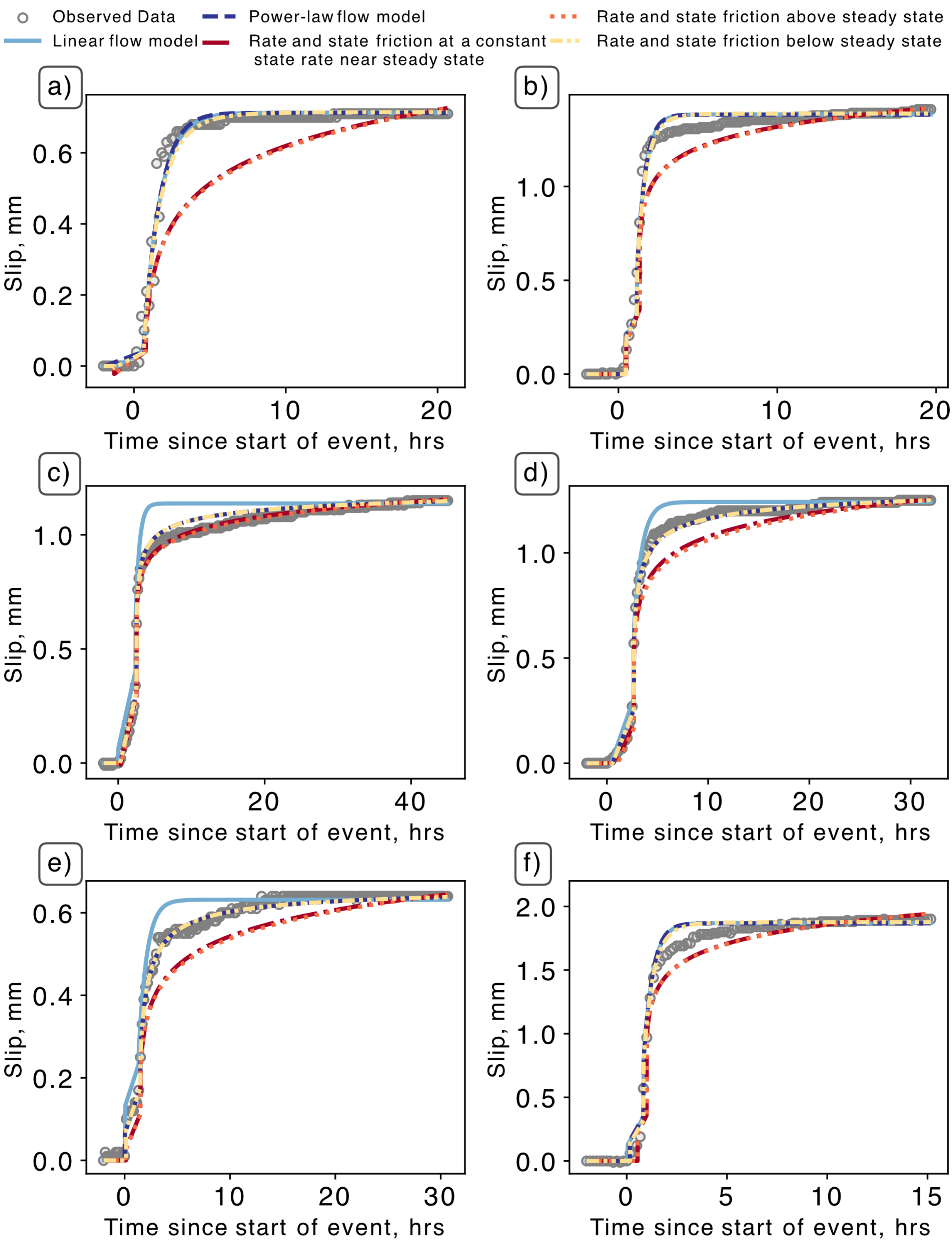

Figure 6 Six example events showing the five rheological fits. a) XHR 004, b) XHR 030, c) XHR 064, d) XHR 072, e) XHR 088 & f) XHR 105. Note that event codes refer to the events in the catalogue of Gittins and Hawthorne (2022). The observed creepmeter data are grey circles. Linear flow and power-law flow are in light and dark blue, respectively. For the rate and state friction laws, the constant state rate near the steady state is in red, the above steady state is in orange, and the below steady state is in yellow.

5.3.1 Power-law flow

The Akaike weights analysis suggests that power-law flow is the best model. This model has a support across bootstrapped samples of between 37–44% with 70% confidence, with a median support of 41% (Figure 7a, dark blue histogram).

If we remove the competition between power-law

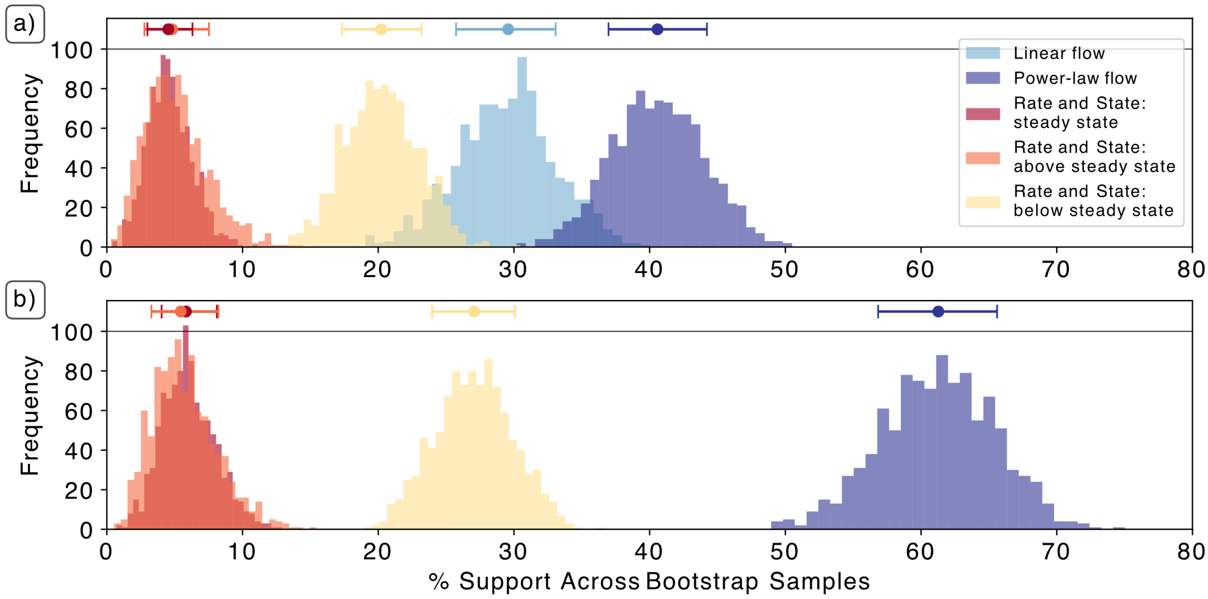

Figure 7 a) Distributions of bootstrap support for each model (linear flow: light blue, power-law flow: dark blue, rate and state friction near steady state: red, rate and state friction above steady state: orange, rate and state friction near steady state: yellow). Scatter points above the histograms represent median value with the 70% confidence intervals on each distribution shown as error bars. b) a) Distributions of bootstrap support for each model with linear flow removed. (power-law flow: dark blue, rate and state friction near steady state: red, rate and state friction above steady state: orange, rate and state friction near steady state: yellow). Scatter points above the histograms represent median value with the 70% confidence intervals on each distribution shown as error bars.

flow and linear flow (nested model where $n = 1$), then power-law flow has a support across bootstrapped samples that increases to between 57–66% with 70 % confidence, with a median support of 61% (Figure 7b, dark blue histogram). This suggests that power-law flow was often competing against the nested linear flow version for the best supported model.

This model works well because it can capture the initial steep gradient of the creep event and its transition through the relatively sharp bend into the relatively flat portion at the end of the events (Figure 6 a, d & e).

5.3.2 Linear flow model

The second best fitting is the linear flow model. Like power-law flow, linear flow is able to capture the sharp bend in the creep events.

Linear flow has fewer parameters than both power-law flow and rate and state friction below steady state; its AIC benefits from the fewer parameters. This model has a support across bootstrapped samples of between 26–33%, with a median support of 30% (Figure 7a, light blue histogram).

5.3.3 Rate and state friction below steady state

The third best rheological model is rate and state friction below steady state. Much like the power-law and linear flow models, the rate and state friction below steady state model can capture the creep event's steep initial gradient, bend, and deceleration. This model has a support across bootstrapped samples of between 17–23%, with a median support of 20% (Figure 7a, yellow histogram).

If we remove the competition between power-law flow and linear flow (nested model where $n = 1$) then the rate and state friction below steady state model has a support across bootstrapped samples of between 24–30% with 70 % confidence, with a median support of 27% (Figure 7b, yellow histogram).

On average then, the below steady state model fits the data slightly worse than power-law flow. However, the two modelled displacements are often very similar (compare the dark blue and yellow lines in Figure 6).

5.3.4 Rate and state friction above steady state

The fourth best model is rate and state friction above steady state. This model has a support across bootstrapped samples of between 3–8%, with a median support of 5% (Figure 7a, orange histogram).

If we remove the competition between power-law flow and linear flow (nested model where $n = 1$), then the rate and state friction above steady state model has very little change in support across bootstrapped samples of between 4–8% with 70 % confidence, with a median support of 6% (Figure 7b, orange histogram).

Despite capturing the first few hours of the event well, the rate and state friction above steady state model fails to capture the bend of the creep event (i.e., the transition from accelerating to decelerating). The observed bend is often much sharper than the model allows. This failure to turn also results in an inability to flatten quickly enough, so the modelled displacements are steeper than the observed displacements at the end of many events.

5.3.5 Rate and state friction near steady state

The model with the least support is the rate and state friction near steady state model. This model is physically intuitive, but it does not match the evolution of slip well. It has support across bootstrapped samples of only between 3–6%, with a median support of 5% (Figure 7a, red histogram).

Much like the above steady state model, the near steady state model shows little to no change in model support once linear flow is removed. In this case, this model has a support across bootstrapped samples of between 3–8% with 70 % confidence, with a median support of 5% (Figure 7b, red histogram).

This model suffers from the same drawbacks as the rate and state friction above steady state. The modelled displacements cannot turn sharply enough or flatten off quickly enough to match the data (red lines in Figure 6).

6 Best-fitting model parameters

To get a further plausibility check and to learn more about the properties of the system, we investigate the individual parameters needed to match the data (Figure 8). Figure 8 shows the distribution of parameters obtained from the best fitting models for each rheology from the collection of events used.

The first column of Figure 8 shows the distribution of the initial slip rate V_0 for each rheological model. The distributions are all similar; they have peaks near V_0 =1 – 2 $\times$ 10^{-7} ms^{-1} but then stay relatively flat until 10^{-6} ms^{-1}. The similarity of these distributions may also explain why most of the fits in Figure 6 do a relatively good job of explaining the beginning of the creep event; they all reasonably match the initial slip rate.

The second column in Figure 8 shows the distribution of the various 'time constants'. These time constants control the rate at which the laws can turn and flatten off during deceleration. Most of these time constants are below 1 hour, except for rate and state below steady state, which has time constants up to 10 hours (note the change in x-axis limits in Figure 8l).

The remaining panels in Figure 8 show the distributions of any other fitting parameters used, notably n for the power-law flow law (panel e) and b/a for the below steady state model (panel m). The rate and state friction below steady state law (Equation 10) uses the ratio of the two rate and state coefficients, b/a (panel m, bottom row). If this ratio is below 1, the fault is velocity-strengthening, whereas if b/a is above 1, the fault is velocity-weakening. From Figure 8 m, we can see that for the majority of events, $b/a > 1$ (vertical grey dashed line). This could suggest that the fault is largely within a velocity-weakening regime, is sensible for this model (see brown arrow in Figure 4b). However, as seen in Figure 8m, 3 out of 50 events are best fit by $b/a < 1$. It is difficult to know whether to interpret these three values. We note that this evolution is still physically possible if a creep event were driven by surrounding slip and abruptly slowed down (Kanu and Johnson, 2011).

The power-law model uses a different parameter, the power-law constant n. Most of the best-fitting n values are below 2. The median value obtained when the power-law model is competitive ($\Delta AIC \leq 2$) is 0.97, lower than the 1.6 estimated by Crough and Burford (1977) for their empirical power-law fit. 49% of n values are between 0.9–1.1, with 41% between 0.9–1. So many events close to 1 suggests that fits may be linear flow, given that this is a special case of the power-law flow model with n = 1. The closeness of the two flow laws is also seen in Figure 6, where they occasionally lie on top of one another. This is the main reason we chose to consider the Akaike weights with and without linear flow (Figure 7), as to not down-weight the model support for power-law flow as it was competing with a special version of itself.

It is somewhat interesting to consider the parameters obtained from the different models for individual creep events. Plotting n against b/a (Figure 9) reveals that events that have higher values of n when modelled with power law flow have lower values of b/a with modelled with rate and state friction below steady state.

7 Discussion

We fit five rheological models to creepmeter data from Harris Ranch, CA. Two models fit the data poorly: rate and state friction above steady state, and rate and state friction near steady state. These models cannot capture the strong change in slip rate, or the bend in the observed slip.

The top three models match the data almost equally well. These are a power-law flow, linear flow, and rate and state friction below steady state.

In Sections 7.1 & 7.2, we discuss the best-fitting models' implications for the dynamics of creep events. In Section 7.3, we recognise that the rheological models we test are simple and that more complex models may be better suited to describing the displacement in creep events. We discuss some potential origins of this complexity.

7.1 Option 1: Power-law flow and Linear flow

In the power-law flow model, slip rate $\propto$ applied stress^n. The fact that this model matches the data would suggest that the shallow fault obeys this rheology. Such a rheology is surprising, as power-law flow is typically reserved for modelling ductile behaviour at depth (Montési, 2004; Passchier and Trouw, 2005). Creep events occur near and at the surface (e.g., Bilham and Behr, 1992; Gladwin et al., 1994; Mortensen et al., 1977; Wei et al., 2013), at depths much shallower than the brittle-ductile transition (e.g., Sibson, 1977). Therefore, one would expect them to occur from a brittle process.

However, ductile deformation can occur in diagenetic conditions if fluids are abundant: via pressure solution creep, where stress variations drive mass transfer (Passchier and Trouw, 2005). Pressure solution creep sometimes results in a slip rate-stress relationship similar to that from deeper deformation mechanism as defined in Equation 11. It accommodates fault creep by grain-boundary sliding through diffusion creep (Gratier et al.,

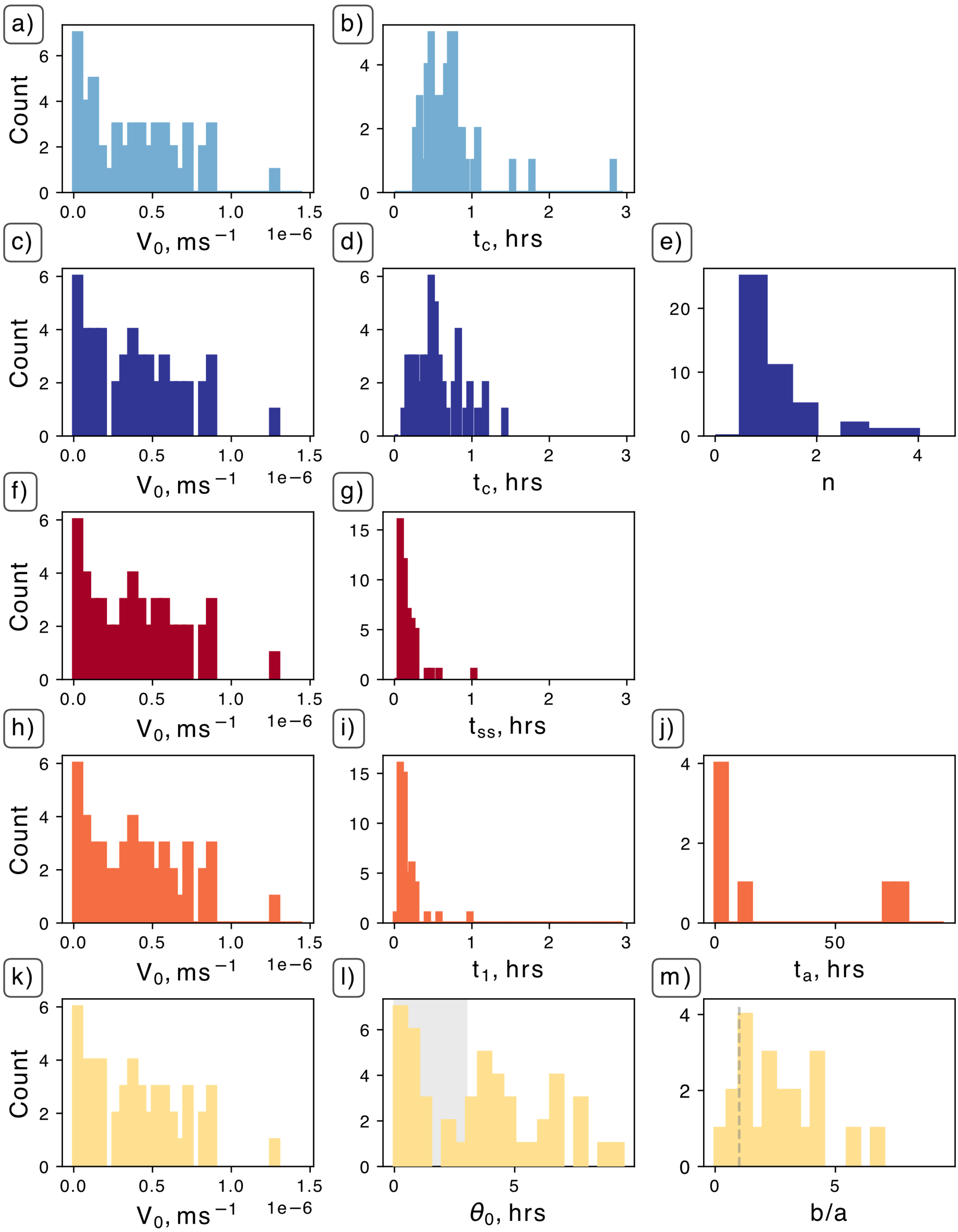

Figure 8 Distributions of the fitting parameters with one value per creep event. a) & b) are the initial slip rate and time constant of the linear flow law. c), d), and e) are the power-law flow law's initial slip rate, time constant, and power-law exponent. f) & g) are the initial slip rate and time constant of the rate and state friction at a constant state rate near steady state. h), i) & j) are the initial slip rate, time constant, and time of tectonic loading in the rate and state friction law above steady state. k), l), and m) are the initial slip rate, time constant, and the ratio of the rate and state coefficients b/a of the rate and state friction law below the steady state.

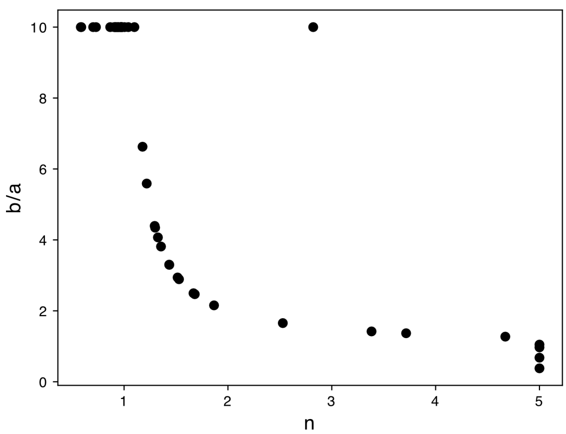

Figure 9 Scatter plot of power-law flow n against Rate and State friction - below steady state b/a.

2011). During pressure solution creep, material is dissolved from grain boundaries at sites of high stress and thus solubility. The material diffuses down a stress-induced chemical potential gradient to be redeposited at nearby sites of low solubility (Gratier et al., 2013; Passchier and Trouw, 2005; Richard et al., 2014).

Evidence for pressure solution creep within fault sections known to creep has been observed in rock samples collected from the San Andreas Fault Observatory at Depth (SAFOD) (Gratier et al., 2011; Richard et al., 2014). Here, microstructural analysis gives evidence for stress-driven dissolution of quartz and feldspars at quartz-feldspar grain impingements along pressure solution seams (Gratier et al., 2011). Phyllosilicates are passively concentrated along these pressure solution seams, leading to up to 50–70% phyllosilicates in rock samples from the actively creeping zone of the SAFOD drill core (Gratier et al., 2011; Richard et al., 2014) compared to 10% in the surrounding rocks outside of the actively creeping zone (Richard et al., 2014; Solum et al., 2006). These phyllosilicates are predominantly saponite, a frictionally weak mineral used to explain the low frictional strength of the San Andreas Fault (Lockner et al., 2011; Moore and Rymer, 2012). At the SAFOD site, diffusion-accommodated grain boundary sliding alone is able to accommodate the 20 mmyr^{-1} creep rate (Gratier et al., 2011).

However, even if pressure solution creep can accommodate the 20 mmyr^{-1} ($\sim 6\times 10^{-10}$ ms^{-1}) long-term creep rate on the San Andreas Fault (Gratier et al., 2011), creep events often have higher slip speeds, of order 10^{-7} ms^{-1} – 10^{-6} ms^{-1}. At these slip rates, pressure solution creep will need to compete with other deformation mechanisms, such as frictional slip. Further, the material transported by pressure solution may be offset by dilation of the fault zone due to granular flow (Niemeijer and Spiers, 2006). Dilatancy has been observed during creep events using a series of orthogonal creepmeters along the San Andreas Fault (Bilham et al., 2021) and is thought to be accommodated by the rotation of large lens-shaped clay clasts (phacoids) found along the creeping faults (Bilham and Castillo, 2019). This dilation should not be surprising given that shear strain results in dilatancy of granular materials (Kruyt and Rothenburg, 2016). More work is required to assess the interplay of pressure solution creep and dilation due to granular flow, and thus to assess whether it is physically plausible that pressure solution creep accommodates slip during creep events, and to assess whether another physical model could follow a power-law flow rheology.

7.2 Option 2: Rate and state friction below steady state in a velocity-weakening regime

The other model that matches the data relatively well is rate and state friction below steady state, with parameters implying a velocity-weakening material. This model is also slightly unintuitive, as one must explain how a fault suddenly reaches a below steady state regime. Typically faults drop below steady state *after* some slip and a drop in stress. Indeed, the below steady state model assumes that stress is constant in time as the fault slows down.

To explain the fit by rate and state friction below steady state, we propose a simple scenario. Perhaps at the surface, we only observe the end of a larger creep event. The near-surface portion of the fault may be weaker than the fault at depth. In this case, the near-surface can maintain small changes in stress, and near-surface slip will closely track slip at depth, so that there are minimal spatial variations in slip and thus minimal stresses. This process would function for $a < b$ and $a > b$.

One could imagine a sequence of events that produces below-steady-state slip evolution. A small velocity-weakening patch at depth may nucleate a creep event. This slip may initially create the ~hour-long strain offsets that have been observed to occur prior to creep events in the region (Gittins and Hawthorne, 2024). The slip then propagates spatially. By the time slip reaches the surface, we are near the end of the creep event. The surface slip follows the slip at depth, with the whole fault slowing down everywhere with a modest change in stress.

Of course, this scenario is simple and speculative. For the scenario to explain the observed evolution in slip, the fault would likely have to have a particular distribution of shallow and deeper strengths. In particular, the near-surface layer would require a low enough normal stress to provide only a modest resistance to acceleration. Further modelling and testing is required to assess whether the assumption of a zero change in stress is truly plausible.

7.3 Option 3: More complex model required?

In all of our model testing, we have taken a rather simplistic approach. We have considered single, simple rheologies, and we have assumed that the spatial distribution of slip remains constant through time. This seems an appropriate starting point for assessing rheological models. However, the analytical approximations we use constrain our modelling abilities. Further, creep events could have more complex rheologies or more complex spatial distributions of slip.

7.3.1 Should the onset and decay of the creep event be modelled separately?

We have attempted to model the acceleration and deceleration in a creep event with a single analytical approximation by modelling the displacement resulting from a step in stress. That approximation is reasonable for the viscous flow models, where the "state" of the fault is unchanged through time. However, it may be that we should have switched rate and state regime during the creep event. It is plausible that the fault is well above steady state in the beginning of the creep event but that it decays and falls close to or below steady state toward the event end.

Such a change in regime would be consistent with the spatial growth of creep events. For instance, if a creep event nucleates at depth and propagates to the surface, the surface will receive a rapid increase in stress as the slip front arrives, causing the surface to accelerate and move well above steady state. Then, when the creep event reaches its final size, the whole fault system decelerates together; it may fall below steady state.

Testing this process in practice is not as simple as splitting the creep event in to two halves, an acceleration and deceleration phase, because creep events are more complex and are comprised of multiple different phases.

Note that the the straight line we fit in Equation 14 does not accommodate an acceleration phase within the creep event. It exists to account for the observation that many creep events are often preceded by a displacement related to the approach of a subsurface dislocation before the commencement of slip at the creepmeter site (King et al., 1977). This displacement phase, often termed the preamble, arises from a transition from a distributed shear strain to discrete slip of the surface fault. This occurs when strain exceeds $\approx 10^{-5}$ or $\approx$100 μm in a 10 m long creepmeter. The transition from strain to slip typically occurs within 5 minutes, less than the spacings between the samples at the Harris Ranch creepmeter site and is not captured in the creepmeter records here.

Following the onset of the creep event, the peak slip velocity is often reached within 20–30 minutes, or 2–3 data points. Therefore most models are able to capture this phase well. In order to model the acceleration and deceleration phases of creep events more robustly, creepmeter data at higher sampling rates would be required.

7.3.2 Does the fit require more complex rheologies?

In our modelling, we choose five simple rheologies, which represent physically plausible approximations of the fault's strength. However, all of the proposed models may be considered counter-intuitive, as they all require some external 'kick' to initiate a creep event; these rheologies do not give rise to creep events spontaneously. Such a kick is plausible, for example as a result of slip at depth (Gittins and Hawthorne, 2024). However, it is also possible that creep events are self-driven, even near the surface

For the creep events to be self-driven one could envision that a small-velocity weakening patch could be loaded by background fault motion and cause a spontaneous acceleration. The slip rate in a creep event could be limited by other important fault zone processes such as dilatancy and pore pressure changes (Iverson, 2005; Segall and Rice, 1995; Segall et al., 2010). Dilatancy could significantly change the functional form of some of the rate and state friction laws, making them able to fit the data better. While it is not obvious that including dilatancy would improve the fit to the data, it is possible, and there is evidence for fault zone dilation during creep events. There are water well level changes when creep events propagate past (Roeloffs et al., 1989; Rudnicki et al., 1993), measurements from orthogonal creepmeter setups (Bilham et al., 2021), and the proposed rotation during creep events of lens-shaped clay clasts found within the core of creeping faults at the surface (Bilham and Castillo, 2019). Dilation is indeed plausible given the local material properties; bursts of slip preceding creep events often occur below 4 km depth (Gittins and Hawthorne, 2024), which places them at similar depths to the extent of the unconsolidated sedimentary sequence deposited since the Early Pliocene (Allen et al., 1946; Dibblee, 2006; Rogers, 1980), and shear strain commonly results in dilatancy in granular materials (Kruyt and Rothenburg, 2016).

Additional work is required to (1) incorporate more complex rheologies, and (2) develop models that fit different parts of the full creep event cycle.

8 Conclusion

In this study, we have used the displacement time evolution of surface rupturing creep events to help determine the physical process driving them. Using creepmeter data from Harris Ranch, CA, we have minimised the misfit between the observed data and the displacement time evolution of five rheological models: (1) rate and state friction at a constant state rate near steady state, (2) rate and state friction above steady state, (3) rate and state friction below steady state, (4) power-law flow, and (5) linear flow. We find that the "standard" velocity-strengthening friction models do not match the data well. Instead, the data is best described by a power-law flow model or by a rate and state friction below steady state model. This initial test of rheologies for creating creep events suggests several possible implications: (1) power-law creep may somehow dominate even at near-surface conditions, (2) the near-surface may be weak, so that near-surface slip largely mirrors the rheology of deeper slip, or (3) a more complex rheology may be needed, potentially involving dilatancy or pore-pressure evolution.

Acknowledgements

Gittins was supported by the Natural Environment Research Council grant number NE/S007474/1. We thank

Junle Jiang and Eric Lindsey who helped to improve the content and clarity of this manuscript. We are also grateful for continual discussions of creep via the NERC-funded COMET annual meetings and collaborations.

Data and code availability

All creepmeter data in this study was produced by the United States Geological Survey (Langbein et al., 2024) and is available from https://earthquake.usgs.gov/monitoring/deformation/data/download.php. The catalogue of creep events was produced by Gittins and Hawthorne (2022) and is available in the supporting information of that publication. The CreepEventRheology software used to analyse the rheology of creep events is archived on Zenodo and available from Gittins (2025).

Competing interests

The authors acknowledge that there are no conflicts of interest recorded.

References

Akaike, H. Information theory and an extension of the maximum likelihood principle. In Petrov, B. N. and Csaki, F., editors, *Proceedings of the 2nd International Symposium on Information Theory*, pages 267–281. Akademiai Kiado, Budapest, 1973.

Akaike, H. Information Theory and an Extension of the Maximum Likelihood Principle. In Parzen, E., Tanabe, K., and Kitagawa, G., editors, *Selected Papers of Hirotugu Akaike*, pages 199–213. Springer, New York, NY, 1998. doi: 10.1007/978-1-4612-1694-0_15.

Allen, J. E., Fowle, R. E., and California, Division of Mines. *Geology of the San Juan Bautista quadrangle, California*. Number 112 p. California Division of Mines, Geologic Branch, San Francisco, 1946. //catalog.hathitrust.org/Record/100088659.

Ampuero, J.-P. and Rubin, A. M. Earthquake nucleation on rate and state faults – Aging and slip laws. *Journal of Geophysical Research*, 113(B1):B01302, 2008. doi: 10.1029/2007JB005082.

Beeler, N. M., Tullis, T. E., and Weeks, J. D. The roles of time and displacement in the evolution effect in rock friction. *Geophysical Research Letters*, 21(18):1987–1990, 1994. doi: 10.1029/94GL01599.

Bhattacharya, P., Rubin, A. M., Bayart, E., Savage, H. M., and Marone, C. Critical evaluation of state evolution laws in rate and state friction: Fitting large velocity steps in simulated fault gouge with time-, slip-, and stress-dependent constitutive laws. *Journal of Geophysical Research: Solid Earth*, 120(9):6365–6385, 2015. doi: 10.1002/2015JB012437.

Bhattacharya, P., Rubin, A. M., and Beeler, N. M. Does fault strengthening in laboratory rock friction experiments really depend primarily upon time and not slip? *Journal of Geophysical Research: Solid Earth*, 122(8):6389–6430, 2017. doi: 10.1002/2017JB013936.

Bilham, R. and Behr, J. A two-layer model for aseismic slip on the Superstition Hills fault, California. *Bulletin of the Seismological Society of America*, 82(3):1223–1235, 1992. doi: 10.1785/BSSA0820031223.

Bilham, R. and Castillo, B. Triggered slip and afterslip in the 2019 Ridgecrest earthquakes: influence of fault zone fabric. *Poster Presentation at 2019 SCEC Annual Meeting*, 2019.

Bilham, R., Suszek, N., and Pinkney, S. California Creepmeters. *Seismological Research Letters*, 75(4):481–492, 2004. doi: 10.1785/gssrl.75.4.481.

Bilham, R., Ozener, H., Mencin, D., Dogru, A., Ergintav, S., Cakir, Z., Aytun, A., Aktug, B., Yilmaz, O., Johnson, W., and Mattioli, G. Surface creep on the North Anatolian Fault at Ismetpasa, Turkey, 1944–2016. *Journal of Geophysical Research: Solid Earth*, 121 (10):7409–7431, 2016. doi: 10.1002/2016JB013394.

Bilham, R., Langbein, J. O., Ericksen, T. L., Nevitt, J. M., Brooks, B. A., and Mencin, D. J. Fault-zone gas venting and aseismic slip: ventilation or lubrication? *Poster Presentation at 2021 SCEC Annual Meeting.*, 2021.

Burford, R. O. Bimodal distribution of creep event amplitudes on the San Andreas fault, California. *Nature*, 268(5619):424–426, 1977. doi: 10.1038/268424a0.

Crough, S. T. and Burford, R. O. Empirical law for fault-creep events. *Tectonophysics*, 42(1):T53–T59, 1977. doi: 10.1016/0040-1951(77)90024-5.

Dibblee, T. W. Geologic map of the Hollister quadrangle, Monterey & San Benito Counties, California, 2006. https://ngmdb.usgs.gov/Prodesc/proddesc_77440.htm. https://ngmdb.usgs.gov/Prodesc/proddesc_77440.htm.

Dieterich, J. H. Modeling of rock friction: 1. Experimental results and constitutive equations. *Journal of Geophysical Research: Solid Earth*, 84(B5):2161–2168, 1979. doi: 10.1029/JB084iB05p02161.

Dieterich, J. H. Earthquake nucleation on faults with rate-and state-dependent strength. *Tectonophysics*, 211(1):115–134, 1992. doi: 10.1016/0040-1951(92)90055-B.

Evans, B. and Kohlstedt, D. L. Rheology of Rocks. In Ahrens, T. J., editor, *Rock Physics and Phase Relations: A Handbook of Physical Constants*, volume 3 of *AGU reference shelf*, pages 148–165. American Geophysical Union, 1995.

Evans, K. F., Burford, R. O., and King, G. C. P. Propagating episodic creep and the aseismic slip behavior of the Calaveras Fault north of Hollister, California. *Journal of Geophysical Research: Solid Earth*, 86(B5):3721–3735, 1981. doi: 10.1029/JB086iB05p03721.

Gittins, D. dbgittins/CreepEventRheology: CreepEventRheology, July 2025. doi: 10.5281/zenodo.16372902.

Gittins, D. B. and Hawthorne, J. C. Are Creep Events Big? Estimations of Along-Strike Rupture Lengths. *Journal of Geophysical Research: Solid Earth*, 127(1):e2021JB023001, 2022. doi: 10.1029/2021JB023001.

Gittins, D. B. and Hawthorne, J. C. Scattered M3–4 Slip Bursts Within Creep Events on the San Andreas Fault. *Journal of Geophysical Research: Solid Earth*, 129(6):e2023JB028187, 2024. doi: 10.1029/2023JB028187.

Gladwin, M. T., Gwyther, R. L., Hart, R. H. G., and Breckenridge, K. S. Measurements of the strain field associated with episodic creep events on the San Andreas Fault at San Juan Bautista, California. *Journal of Geophysical Research: Solid Earth*, 99(B3): 4559–4565, 1994. doi: 10.1029/93JB02877.

Goulty, N. R. and Gilman, R. Repeated creep events on the San Andreas Fault near Parkfield, California, Recorded by a strainmeter array. *Journal of Geophysical Research*, 83(B11):5415, 1978. doi: 10.1029/JB083iB11p05415.

Gratier, J.-P., Richard, J., Renard, F., Mittempergher, S., Doan, M.-L., Di Toro, G., Hadizadeh, J., and Boullier, A.-M. Aseismic sliding of active faults by pressure solution creep: Evidence from the San Andreas Fault Observatory at Depth. *Geology*, 39(12): 1131–1134, Dec. 2011. doi: 10.1130/G32073.1.

Gratier, J.-P., Dysthe, D. K., and Renard, F. The Role of Pressure

Solution Creep in the Ductility of the Earth's Upper Crust. In *Advances in Geophysics*, volume 54, pages 47–179. Elsevier, 2013. doi: 10.1016/B978-0-12-380940-7.00002-0.

Harris, R. A. Large earthquakes and creeping faults. *Reviews of Geophysics*, 55(1):169–198, Mar. 2017. doi: 10.1002/2016RG000539.

Hawthorne, J. C. and Rubin, A. M. Short-time scale correlation between slow slip and tremor in Cascadia. *Journal of Geophysical Research: Solid Earth*, 118(3):1316–1329, Mar. 2013. doi: 10.1002/jgrb.50103.

Helmstetter, A. and Shaw, B. E. Afterslip and aftershocks in the rate-and-state friction law. *Journal of Geophysical Research: Solid Earth*, 114(B1), 2009. doi: 10.1029/2007JB005077.

Hirao, B., Savage, H., and Brodsky, E. E. Communication Between the Northern and Southern Central San Andreas Fault via Dynamically Triggered Creep. *Geophysical Research Letters*, 48 (13):e2021GL092530, 2021. doi: 10.1029/2021GL092530.

Hirth, G. and Kohlstedt, D. Rheology of the Upper Mantle and the Mantle Wedge: A View from the Experimentalists. In *Inside the Subduction Factory*, Geophysical Monograph Series, pages 83–105. American Geophysical Union (AGU), 2004. https://onlinelibrary.wiley.com/doi/abs/10.1029/138GM06.

Iverson, R. M. Regulation of landslide motion by dilatancy and pore pressure feedback. *Journal of Geophysical Research: Earth Surface*, 110(F2), 2005. doi: 10.1029/2004JF000268.

Kanu, C. and Johnson, K. Arrest and recovery of frictional creep on the southern Hayward fault triggered by the 1989 Loma Prieta, California, earthquake and implications for future earthquakes. *Journal of Geophysical Research*, 116(B4):B04403, 2011. doi: 10.1029/2010JB007927.

Khoshmanesh, M., Shirzaei, M., and Nadeau, R. M. Time-dependent model of aseismic slip on the central San Andreas Fault from InSAR time series and repeating earthquakes. *Journal of Geophysical Research: Solid Earth*, 120(9):6658–6679, Sept. 2015. doi: 10.1002/2015JB012039.

King, C.-Y. Kinematics of Slow-Slip Events. In *Earthquakes - Impact, Community Vulnerability and Resilience*. IntechOpen, 2019. doi: 10.5772/intechopen.84904.

King, C.-Y., Nason, R. D., and Tocher, D. Kinematics of Fault Creep. *Philosophical Transactions of the Royal Society of London. Series A, Mathematical and Physical Sciences*, 274(1239):355–360, 1973. http://www.jstor.org/stable/74192.

King, C.-Y., Nason, R. D., and Burford, R. O. Coseismic steps recorded on creep meters along the San Andreas Fault. *Journal of Geophysical Research (1896-1977)*, 82(11):1655–1662, 1977. doi: 10.1029/JB082i011p01655.

Kraft, D. A software package for sequential quadratic programming. Tech. Rep. DFVLR-FB 88-28, DLR German Aerospace Center — Institute for Flight Mechanics, Koln, Germany, 1988.

Kruyt, N. P. and Rothenburg, L. A micromechanical study of dilatancy of granular materials. *Journal of the Mechanics and Physics of Solids*, 95:411–427, Oct. 2016. doi: 10.1016/j.jmps.2016.01.019.

Langbein, J. Noise in two-color electronic distance meter measurements revisited. *Journal of Geophysical Research: Solid Earth*, 109(B4), 2004. doi: 10.1029/2003JB002819.

Langbein, J. and Johnson, H. Correlated errors in geodetic time series: Implications for time-dependent deformation. *Journal of Geophysical Research: Solid Earth*, 102(B1):591–603, 1997. doi: 10.1029/96JB02945.

Langbein, J., Quilty, E., and Breckenridge, K. Sensitivity of crustal deformation instruments to changes in secular rate. *Geophysical Research Letters*, 20(2):85–88, 1993. doi: 10.1029/92GL02718.

Langbein, J., Bilham, R. G., Snyder, H., and Ericksen, T. L. Summary of Creepmeter Data from 1980 to 2020—Measurements Spanning the Hayward, Calaveras, and San Andreas Faults in Northern and Central California. Open-File Report, USGS, Renton, Virginia, 2024. Series: Open-File Report DOI: 10.3133/ofr20241011.

Lawson, C. L. and Hanson, R. J. 25. Practical Analysis of Least Squares Problems. In *Solving Least Squares Problems*, Classics in Applied Mathematics, pages 180–198. Society for Industrial and Applied Mathematics, Jan. 1995. doi: 10.1137/1.9781611971217.ch25.

Lockner, D. A., Morrow, C., Moore, D., and Hickman, S. Low strength of deep San Andreas fault gouge from SAFOD core. *Nature*, 472 (7341):82–85, 2011. doi: 10.1038/nature09927.

Lyons, S. and Sandwell, D. Fault creep along the southern San Andreas from interferometric synthetic aperture radar, permanent scatterers, and stacking. *Journal of Geophysical Research: Solid Earth*, 108(B1), Jan. 2003. doi: 10.1029/2002JB001831.

Marone, C. J., Scholtz, C. H., and Bilham, R. On the mechanics of earthquake afterslip. *Journal of Geophysical Research: Solid Earth*, 96(B5):8441–8452, 1991. doi: 10.1029/91JB00275.

Mchugh, S. and Johnston, M. J. S. Short-period nonseismic tilt perturbations and their relation to episodic slip on the San Andreas Fault in central California. *Journal of Geophysical Research (1896-1977)*, 81(35):6341–6346, 1976. doi: 10.1029/JB081i035p06341.

Montési, L. G. J. Controls of shear zone rheology and tectonic loading on postseismic creep. *Journal of Geophysical Research: Solid Earth*, 109(B10), 2004. doi: 10.1029/2003JB002925.

Moore, D. E. and Rymer, M. J. Correlation of clayey gouge in a surface exposure of serpentinite in the San Andreas Fault with gouge from the San Andreas Fault Observatory at Depth (SAFOD). *Journal of Structural Geology*, 38:51–60, 2012. doi: 10.1016/j.jsg.2011.11.014.

Mortensen, C. E., Lee, R. C., and Burford, R. O. Observations of creep-related tilt, strain, and water-level changes on the central San Andreas fault. *Bulletin of the Seismological Society of America*, 67(3):641–649, 1977. doi: 10.1785/BSSA0670030641.

Nadeau, R. M. and McEvilly, T. V. Periodic Pulsing of Characteristic Microearthquakes on the San Andreas Fault. *Science*, 303(5655): 220–222, 2004. doi: 10.1126/science.1090353.

Nason, R. and Weertman, J. A dislocation theory analysis of fault creep events. *Journal of Geophysical Research (1896-1977)*, 78 (32):7745–7751, 1973. doi: 10.1029/JB078i032p07745.

Nason, R. D., Philippsborn, F. R., and Yamashita, P. A. Catalog of creepmeter measurements in central California from 1968 to 1972. Technical Report 74-31, U.S. Geological Survey, 1974. doi: 10.3133/ofr7431. Publication Title: Open-File Report.

Nelder, J. A. and Mead, R. A Simplex Method for Function Minimization. *The Computer Journal*, 7(4):308–313, Jan. 1965. doi: 10.1093/comjnl/7.4.308.

Niemeijer, A. R. and Spiers, C. J. Velocity dependence of strength and healing behaviour in simulated phyllosilicate-bearing fault gouge. *Tectonophysics*, 427(1):231–253, 2006. doi: 10.1016/j.tecto.2006.03.048.

Nocedal, J. and Wright, S. J. *Numerical Optimization*. Springer Series in Operations Research and Financial Engineering. Springer New York, 2006. doi: 10.1007/978-0-387-40065-5.

Passchier, C. W. and Trouw, R. A. J. *Microtectonics*. Springer, Berlin ; New York, 2nd rev. and enl. ed. edition, 2005.

Perfettini, H. and Avouac, J.-P. Postseismic relaxation driven by brittle creep: A possible mechanism to reconcile geodetic measurements and the decay rate of aftershocks, application to the Chi-Chi earthquake, Taiwan. *Journal of Geophysical Research:*

Solid Earth, 109(B2), 2004. doi: 10.1029/2003JB002488.

Richard, J., Gratier, J.-P., Doan, M.-L., Boullier, A.-M., and Renard, F. Rock and mineral transformations in a fault zone leading to permanent creep: Interactions between brittle and viscous mechanisms in the San Andreas Fault. *Journal of Geophysical Research: Solid Earth*, 119(11):8132–8153, 2014. doi: 10.1002/2014JB011489.

Roeloffs, E. A. Creep rate changes at Parkfield, California 1966–1999: Seasonal, precipitation induced, and tectonic. *Journal of Geophysical Research: Solid Earth*, 106(B8):16525–16547, 2001. doi: 10.1029/2001JB000352.

Roeloffs, E. A., Burford, S. S., Riley, F. S., and Records, A. W. Hydrologic effects on water level changes associated with episodic fault creep near Parkfield, California. *Journal of Geophysical Research: Solid Earth*, 94(B9):12,387–12,402, 1989. doi: 10.1029/JB094iB09p12387.

Rogers, T. Geology and seismicity at the convergence of the San Andreas and Calaveras fauft zones near Hollister, San Benito County, California. In Sherburne, R. W. and Streitz, R., editors, *Studies of the San Andreas Fault zone in Northern California*, pages 19–28. Sacramento CA : California Division of Mines and Geology, 1980. http://archive.org/details/studiesofsanandr140cali.

Rubin, A. M. and Ampuero, J.-P. Earthquake nucleation on (aging) rate and state faults. *Journal of Geophysical Research: Solid Earth*, 110(B11), Nov. 2005. doi: 10.1029/2005JB003686.

Rudnicki, J. W., Yin, J., and Roeloffs, E. A. Analysis of water level changes induced by fault creep at Parkfield, California. *Journal of Geophysical Research: Solid Earth*, 98(B5):8143–8152, 1993. doi: 10.1029/93JB00354.

Ruina, A. Slip instability and state variable friction laws. *Journal of Geophysical Research: Solid Earth*, 88(B12):10359–10370, 1983. doi: 10.1029/JB088iB12p10359.

Scholz, C. H. *The Mechanics of Earthquakes and Faulting*. Cambridge University Press, New York, 1990.

Scholz, C. H. Earthquakes and friction laws. *Nature*, 391(6662): 37–42, 1998. doi: 10.1038/34097.

Schulz, S. S. Catalog of creepmeter measurements in California from 1966 through 1988. U.S. Geol. Surv. Open File Rep 89-650, U.S. Geological Survey, 1989. Series: Open-File Report.

Schulz, S. S., Burford, R. O., and Mavko, B. Influence of seismicity and rainfall on episodic creep on the San Andreas Fault System in central California. *Journal of Geophysical Research: Solid Earth*, 88(B9):7475–7484, 1983. doi: 10.1029/JB088iB09p07475.

Segall, P. and Rice, J. R. Dilatancy, compaction, and slip instability of a fluid-infiltrated fault. *Journal of Geophysical Research: Solid Earth*, 100(B11):22155–22171, 1995. doi: 10.1029/95JB02403.

Segall, P., Rubin, A. M., Bradley, A. M., and Rice, J. R. Dilatant strengthening as a mechanism for slow slip events. *Journal of Geophysical Research: Solid Earth*, 115(B12), 2010. doi: 10.1029/2010JB007449.

Sibson, R. H. Fault rocks and fault mechanisms. *Journal of the Geological Society*, 133(3):191–213, Mar. 1977. doi: 10.1144/gsjgs.133.3.0191.

Slater, L. E. and Burford, R. O. A comparison of long-baseline strain data and fault creep records obtained near Hollister, California. *Tectonophysics*, 52(1):481–496, 1979. doi: 10.1016/0040-1951(79)90263-4.

Solum, J. G., Hickman, S. H., Lockner, D. A., Moore, D. E., van der Pluijm, B. A., Schleicher, A. M., and Evans, J. P. Mineralogical characterization of protolith and fault rocks from the SAFOD Main Hole. *Geophysical Research Letters*, 33(21), 2006. doi: 10.1029/2006GL027285.

Steinbrugge, K. V. and Zacher, E. G. Fault creep and property damage. *Bulletin of the Seismological Society of America*, 50(3): 389–396, 1960. doi: 10.1785/BSSA0500030389.

Thurber, C. and Sessions, R. Assessment of Creep Events as Potential Earthquake Precursors: Application to the Creeping Section of the San Andreas Fault, California. *Pure and Applied Geophysics*, 152(4):685–705, Nov. 1998. doi: 10.1007/s000240050172.

Tocher, D. Creep rate and related measurements at vineyard, California. *Bulletin of the Seismological Society of America*, 50(3): 396–404, 1960. doi: 10.1785/BSSA0500030389.

USGS and CGS. Quaternary fault and fold database for the United States, 2020. https://www.usgs.gov/programs/earthquake-hazards/faults. Dataset.

Wagenmakers, E.-J. and Farrell, S. AIC model selection using Akaike weights. *Psychonomic Bulletin & Review*, 11(1):192–196, Feb. 2004. doi: 10.3758/BF03206482.

Wei, M., Kaneko, Y., Liu, Y., and McGuire, J. J. Episodic fault creep events in California controlled by shallow frictional heterogeneity. *Nature Geoscience*, 6(7):566–570, 2013. doi: 10.1038/ngeo1835.

Wesson, R. L. Dynamics of fault creep. *Journal of Geophysical Research*, 93(B8):8929, 1988. doi: 10.1029/JB093iB08p08929.

Whitten, C. A. and Claire, C. N. Analysis of geodetic measurements along the San Andreas Fault. *Bulletin of the Seismological Society of America*, 50(3):404–415, 1960. doi: 10.1785/BSSA0500030389.

Williams, S. D. P., Bock, Y., Fang, P., Jamason, P., Nikolaidis, R. M., Prawirodirdjo, L., Miller, M., and Johnson, D. J. Error analysis of continuous GPS position time series. *Journal of Geophysical Research: Solid Earth*, 109(B3), 2004. doi: 10.1029/2003JB002741.